Effects of high-energy Pb-ion irradiation on critical current and flux pinning in Fe(Se,Te) thin films

Superconductor
Science and
Technology

PAPER • **OPEN ACCESS**

Effects of high-energy Pb-ion irradiation on critical current and flux pinning in Fe(Se,Te) thin films

To cite this article: Michela Fracasso *et al* 2025 *Supercond. Sci. Technol.* **38** 105021

OPEN ACCESS
IOP Publishing
Superconductor Science and Technology
Supercond. Sci. Technol. **38** (2025) 105021 (10pp)
https://doi.org/10.1088/1361-6668/ae0fc6

Effects of high-energy Pb-ion irradiation on critical current and flux pinning in Fe(Se,Te) thin films

Michela Fracasso[1], Mario Scuderi[2,*], Elisa Brugaletta[2], Emilio Bellingeri[3], Michela Iebole[3], Andrea Malagoli[3], Alberto Martinelli[3], Nicola Manca[3], Laura Gozzelino[1], Roberto Gerbaldo[1], Gianluca Ghigo[1], Francesco Laviano[1], Daniele Torsello[1], Marina Putti[4] and Valeria Braccini[3]

[1] Department of Applied Science and Technology, Politecnico di Torino and INFN Sez. Torino, Torino, Italy
[2] CNR-IMM, Catania, Italy
[3] CNR-SPIN, Genova, Italy
[4] Physics Department, University of Genova, Genova, Italy

E-mail: mario.scuderi@cnr.it

Received 15 July 2025, revised 22 September 2025
Accepted for publication 6 October 2025
Published 21 October 2025

Abstract

Irradiating a superconductor with ions is a powerful tool to create a controlled distribution of defects in it, with a morphology depending on the energy and the mass of the chosen particle. In this study, high-energy Pb-ion irradiation (1.15 GeV) was performed on Fe(Se,Te) thin films grown on CaF_2 substrates, to introduce columnar defects and to enhance flux pinning capability and critical current density (J_c). The employed fluence was 2.9×10^{11} cm^{-2}, corresponding to a dose equivalent field of 6 T. X-ray diffraction and scanning transmission electron microscopy analyses confirmed an increase of the defect density after irradiation, and the formation of columnar tracks. Despite a slight reduction in the critical temperature (around 1 K), the irradiated samples showed an increase of J_c up to 40%, in magnetic fields close to the dose equivalent field. Irradiation also induces a kink in the irreversibility line, which is consistent with a transition from a low-field single-vortex pinning regime provided by irradiation columnar defects to a high-field collective pinning regime. Accordingly, the analysis of the pinning force evidenced a shift in the peak position after irradiation, which can be associated to the active role of the irradiation tracks. These results demonstrate the effectiveness of irradiation in optimizing the performance of iron-based superconducting films.

Keywords: Fe-based superconductors, high-energy heavy-ion irradiation, Fe(SeTe), thin films, columnar defects, microstructural analysis via STEM

* Author to whom any correspondence should be addressed.

1. Introduction

Since their discovery, iron-based superconductors (IBSs) have attracted the interest of the scientific community working on applied superconductivity [1], as their relatively high superconducting transition temperature T_c, high upper critical fields H_{c2}, and relatively low anisotropy [2, 3] makes them appealing for developing high-field magnets [4].

The Fe-chalcogenide 11 system, which is characterized by the electroneutral FeSe layer, has some advantages over other Fe-based superconductors: it has lower toxicity due to the absence of As, and the simplest crystal structure among IBSs. Although the parent compound FeSe has a T_c as low as 8 K [5], it can be enhanced to about 15 K in bulk materials through Te or S doping [6, 7], up to 21 K in films due to strain [8], and up to 37 K after application of high pressure [9]. Te substitution on Se site also enhances H_{c2} to 50 T at 2 K, lowering at the same time its anisotropy [7, 10]. Additionally, Fe(Se,Te) (FST) exhibits tolerance to relatively high grain boundary angles, enabling the fabrication of practical conductors without the need for highly textured templates [11, 12].

Some attempts to fabricate FST powder-in-tube tapes have been carried out, but they exhibited poor superconducting performances due to the high reactivity of the phase with the metallic sheaths [13, 14]. Simple coated conductor (CC) architectures have been investigated thanks to the straightforward growth of FST films through pulsed laser deposition (PLD) with respect to RE-$Ba_2Cu_3O_{7-x}$ (RE = rare earth, REBCO henceforth) ones [15]. Commercial templates have been employed to successfully grow FST films [16, 17], and meter-long highly *c*-axis-textured FST-CCs conductors were deposited on CeO_2-buffered IBAD (Ion Beam Assisted Deposition)-MgO tapes by reel-to-reel PLD showing J_c above 2 MA cm^{-2} at 4.2 K and self-field [18]. Recently, simplified RABiTS (Rolling-Assisted Biaxially Textured Substrate) architectures have been proposed [19], and we proved that the simplified architecture Ni-W/Zr-doped CeO_2 (MOD)/Fe(Se,Te) is suitable for the manufacturing of iron-based CCs based on a simple, thin, chemically deposited buffer [20–22].

IBS thin films usually contain numerous natural defects. For example, in the Ba-122 system—depending on the processing conditions—the formation of defects such as BaFeO nanopillars [23], stacking faults [24], dislocations [25], and rotating columnar grains [26] are expected. Our FST thin films showed growth-induced defects which, depending on the specific growth parameters, can include grain boundaries of regularly shaped rotated grains, lattice distortions, 2D defects high-mass walls, different Se/Te stoichiometry, all of which behaving as a source of flux pinning [27]. To improve application-relevant parameters such as the in-field J_c properties of various IBSs, artificial pinning centres have been introduced by using techniques like the multilayer approach, PLD target modification, transition metal doping [28–34].

Among other approaches, irradiation has been proven to be a valuable procedure for the introduction of a controlled distribution of defects, tuning the pinning mechanisms and improving J_c and its in-field behaviour. At the same time, irradiation allows defining damage thresholds above which degradation of the superconducting properties occurs, which is crucial for applications where high radiation levels are expected (e.g. fusion) [35]. The defect morphology can suitably be chosen by selecting mass and energy of the impinging particles [36, 37]. For example, MeV and sub-MeV proton irradiations result in the addition of point defects, which was found to produce J_c enhancement even exceeding 50% [15, 38, 39]. An analogous J_c improvement was measured in FST films where isotropic pinning centres with an average diameter of 10–15 nm were generated by 6 MeV Au-ions [40, 41]. A mixed pinning landscape where discontinuous tracks directed along the ion path are surrounded by clusters of point-like defects were instead created in FST single crystals irradiated by a few hundred MeV Au-ions [42] with a general enhancement of J_c both in dc and high frequency regime [43, 44]. On the other hand, continuous columnar defects are expected in the case of irradiation with heavy ions having energy close to or higher than 1 GeV, as observed in other IBSs [43, 45–47].

In this study, we deal with the effect of 1.15 GeV Pb-ion irradiation on 230 nm thick Fe(Se,Te) films grown on CaF_2 substrates. To our best knowledge, this is the first time that the effect of irradiation with particles potentially able to induce continuous columnar tracks has been investigated in iron chalcogenide films. First, the irradiation-induced modification of the lattice structure was investigated via x-ray diffraction (XRD) measurements and scanning transmission electron microscopy (STEM). Then, we focused on the irradiation effects on parameters such as the critical temperature, the irreversibility line and the critical current density, which are crucial for applications. Overall, the interaction of vortices with pinning centres was investigated both before and after ion irradiation.

2. Experimental details

Two twin 230 nm-thick Fe(Se,Te) thin films were grown by PLD on CaF_2(001) single-crystal substrates using a $FeSe_{0.5}Te_{0.5}$ target synthesized with a two-step method [48]. The deposition was performed with a 1024 nm Nd:YAG laser whose parameters were optimized to obtain high-quality epitaxial thin films: 3 Hz repetition rate, 2 J cm^{-2} fluency, 2 mm^2 spot size, and 5 cm substrate-target distance [49]. During deposition, the substrate was heated at 300 °C at the base pressure of the system (10^{-8} mbar).

The as-grown films were patterned by standard UV lithography followed by water-cooled argon ion milling (with an Ar energy of 500 eV). After the milling process, the samples were cleaned by mild sonication in acetone for a few tens of seconds and dried in nitrogen flow [50]. In order to perform transport properties measurements on a defined geometry, one 5×5 mm^2 sample was patterned as Hall bars (having channel size of 20×50 μm^2), while another one, having size of 7×7 mm^2, was patterned as 1×0.6 mm^2 rectangles for

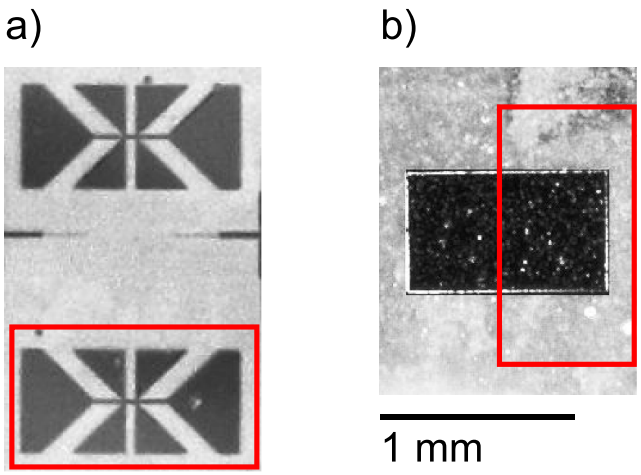

Figure 1. Optical micrographs showing two FST Hall bar-shaped micro-bridges (a), and a rectangular pattern (b). Red boxes delineate the irradiated areas. In the case of the rectangular pattern, half sample was kept in the pristine state by covering it with a tantalum mask.

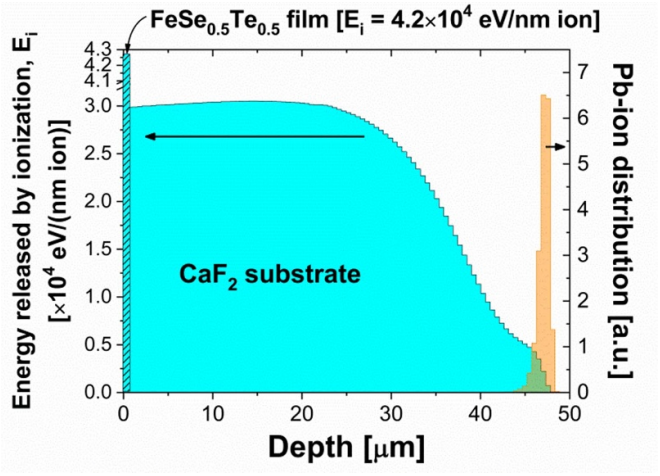

Figure 2. Distribution of the energy lost by Pb-ions due to ionization (i.e. released by inelastic scattering against the target atom electrons) in both the FST film (thickness not to scale) and CaF_2 substrate and Pb-ion implantation peak in the CaF_2 substrate. Data were calculated by means of the Monte Carlo SRIM code. The zero depth corresponds to the sample surface.

XRD analysis. The optical images of both of them are shown in figure 1.

The samples were irradiated in vacuum at room temperature with 1.15 GeV Pb ions at the PIAVE-ALPI facility of the INFN Legnaro National Laboratories (Italy). The irradiation fluence, $\phi = 2.90 \times 10^{11}$ cm^{-2}, corresponds to a dose-equivalent field—i.e. the magnetic field for which the flux-lines density in the sample matches the number of impinging ions per unit area $-B_\phi = 6$ T. The irradiation beam was directed perpendicular to the film plane and the ions implanted into the CaF_2 substrate at a depth of about 47 μm, as calculated by means of the Monte Carlo SRIM code. Among the samples destinated to transport measurements, one Hall bar was homogeneously irradiated (red box area in figure 1(a)), keeping the others in the pristine state. In the case of the rectangular patterns, each one was partially irradiated (red box area in figure 1(b)) and partially kept in the pristine state by shielding it with a tantalum mask. The ions are expected to produce strongly anisotropic columnar defects along the ion's trajectory mainly due to ion inelastic scattering against the target atom electrons (ionization), and a cloud of point-like defects due to secondary collisions [47]. The calculated profile of the implanted ions as well as the distribution of the energy released by inelastic scattering are plotted in figure 2.

XRD measurements were carried out using a Bruker D8 Da Vinci diffractometer, equipped with a two-bounce monochromator for high-resolution measurements and a Montel optic with dual parallelizing mirrors, enabling beam focusing on micrometric regions. The system includes a motorized *XY* stage, an integrated microscope, and a laser alignment system, allowing precise targeting of measurement areas down to 50×50 μm^2.

Two lamellae were extracted by focused ion beam from the irradiated and non-irradiated regions, respectively, of the rectangular-patterned sample shown in figure 1(b). Both regions were selected sufficiently far from the mask edges to ensure that the defect distributions observed in the lamellae are representative of the typical defect landscapes in the irradiated and non-irradiated areas, respectively. These lamellae were analysed by using a JEOL JEM-ARM 200CF microscope. High-angle annular dark field (HAADF) combined with medium-angle annular dark field (MAADF) imaging was used to reveal both mass-thickness contrast and strain fields [51, 52].

Transport measurements on a pristine and an irradiated Hall bar were carried out in a 16 T cryogen-free superconducting magnet with an 85 mm diameter room temperature bore and a variable temperature insert for measurements in the range 1.6–325 K. Resistivity measurements as a function of the applied magnetic field were performed in four-probes configuration. Critical current values at 5 K, 8 K and 12 K and in magnetic fields up to 16 T were extracted from voltage-current characteristics acquired by sweeping the current from zero with exponentially increasing steps. The magnetic field was always applied perpendicular to the film surface and to the bias current path.

3. Results and discussion

High-resolution XRD (HRXRD) measurements were performed on both the irradiated and non-irradiated regions of the FST rectangular pattern shown in figure 1(b), located less than 300 μm apart. Reciprocal space maps were acquired along the [00h] and [h0h] directions to estimate the lattice parameters a and c and θ–2θ sections were extracted and shown in figure 3. Additionally, the Pn–Fe–Pn bond angle (α) and the Pn–Fe bond length (where Pn = Se, Te) were extracted from the intensity ratio of the 001 and 003 reflections, following the method reported in [8].

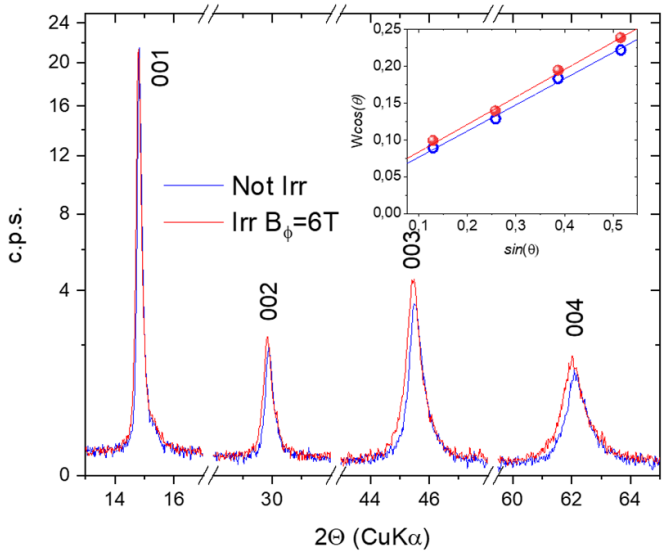

Figure 3. θ–2θ profile of 00l peaks measured in two contiguous regions (pristine and irradiated) of the rectangular pattern shown in figure 1(b). Small but significative variation in position and width are detectable. In the inset the Williamson–Hall plot showing that this broadening reflects an increase in the microstrain and a small reduction in the average coherent domain size.

Rocking curve analysis revealed no significant differences between the irradiated and pristine areas, indicating that the long-range crystalline order remains largely preserved. Nonetheless, slight variations in the lattice parameters were observed, consistent with a modest local distortion (figure 3 shows the superposition of the corresponding diffraction patterns). To assess the impact of irradiation on the microstructural properties of the thin films, a diffraction line broadening analysis was carried out. Although the instrumental contribution to peak broadening was not subtracted—given that our aim was to qualitatively evaluate the effect of irradiation rather than to determine absolute values for strain and crystallite size—the Williamson–Hall analysis of the 00*h* reflections proved informative. In particular, the pristine region yielded a domain size compatible with the film thickness, while a slightly reduced value was found in the irradiated area. As discussed in the following section, this reduction can be attributed to the formation of protrusions at the film–substrate interface, corresponding to ion impact sites, which locally disrupt the coherent scattering volume.

From the differential Williamson–Hall analysis the intercept at the origin confirms the aforementioned reduction in the coherent domain size (D), while the slope reveals an increase in microstrain. These findings indicate that irradiation induces only minimal changes in the average crystallographic structure but generates localized structural distortions. Actually, TEM analysis reveals the formation of irradiation-induced columnar defects accompanied by enhanced microstrain fields (see below), which facilitate the emergence of secondary defects and dislocations, ultimately reducing the size of the coherent domains. Furthermore, the strain fields surrounding these

Table 1. Crystallographic parameters measured in two regions (pristine and irradiated) of the rectangular pattern shown in figure 1(b).

	Pristine	Irradiated
a (Å)	3.736	3.744
c (Å)	5.977	5.979
d Pn–Fe bond length (Å)	2.44	2.46
α Pn–Fe–Pn angle (deg)	99.4	98.8

defects lead to a slight deviation of the Pn–Fe–Pn bond angle, as reflected in the structural parameters reported in table 1, and are likely responsible for the small decrease in the superconducting critical temperature observed after irradiation.

STEM analysis was performed on both irradiated and non-irradiated samples. For the non-irradiated sample, the HAADF-STEM image (figure 4(a)) shows the FST film with a higher contrast than the underlying CaF_2 substrate, in line with the expected Z-contrast arising from its higher average atomic number. The film thickness was measured to be approximately 230 nm. The contrast in the film is not uniform: vertically aligned stripes of varying intensity are clearly visible, indicative of strain fields likely induced by epitaxial mismatch with the CaF_2 substrate. Additionally, several isolated low-contrast dots are dispersed throughout the film, which may correspond to areas with locally disrupted crystalline order.

The MAADF-STEM image (figure 4(b)), acquired from the same region shown in figure 4(a), offers additional insight into the microstructural defects. In particular, the presence of local distortions in the crystal lattice reveals dislocations with different morphologies: some of them appear as localized point-like features (yellow arrows) while others show loop-like configurations (red arrows), both contributing to local strain fields.

The irradiated region was similarly investigated with HAADF and MAADF-STEM imaging (figures 5(a) and (b), respectively). In the HAADF image (figure 5(a)), the overall contrast and structure appear qualitatively similar to the pristine case, with no major changes in morphology. However, at the FST/CaF_2 interface, distinct protrusions are observed and associated to the ion tracks penetrating the substrate. These features, resembling crater-like structures, are likely the result of chemical intermixing and partial diffusion of Ca and F atoms from the substrate into the film and occurring along the ion track as it crosses the film/substrate interface. In contrast, the MAADF-STEM image (figure 5(b)) reveals clear evidence of irradiation-induced damage within the film. In addition to the pre-existing defects observed in the pristine sample, linear features aligned along the ion trajectories are visible throughout the film thickness. These tracks exhibit a central region with contrast similar to the adjoining matrix, surrounded by brighter halos consistent with strain-enhanced contrast. This morphology suggests the presence of columnar defects that consist of partially amorphized columns, with strain fields extending radially outward. Such extended defects are characteristic of ion tracks produced by high-energy heavy ion irradiation and are expected to play a dominant role in flux pinning.

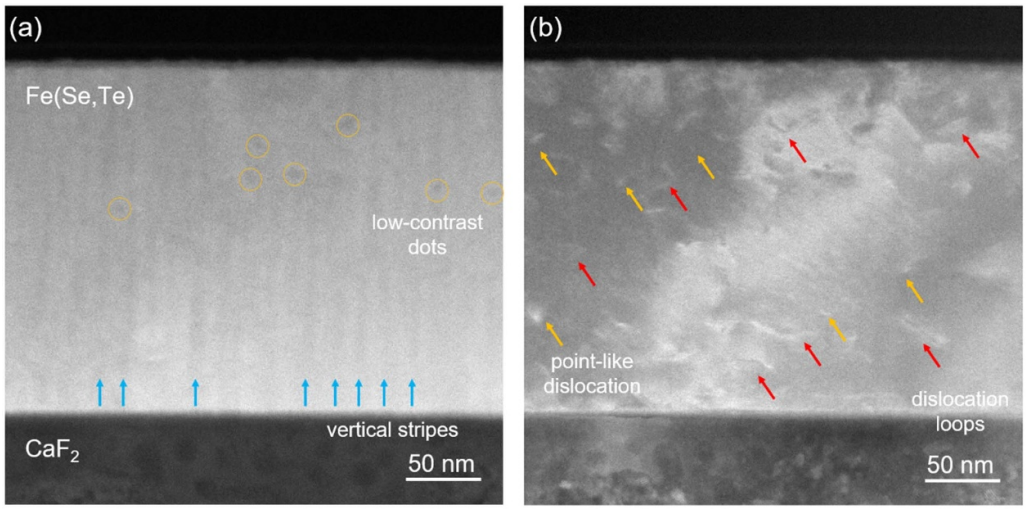

Figure 4. STEM images of the pristine FST film. (a) HAADF-STEM image showing the FST film on CaF_2 substrate. Yellow circles highlight low-contrast dots, while vertical contrast variations throughout the film indicate strain fields due to lattice mismatch with the substrate (blue arrows). (b) MAADF-STEM image of the same region revealing dislocations with different morphologies: point-like features (yellow arrows) and dislocation loops (red arrows) that locally distort the crystal lattice.

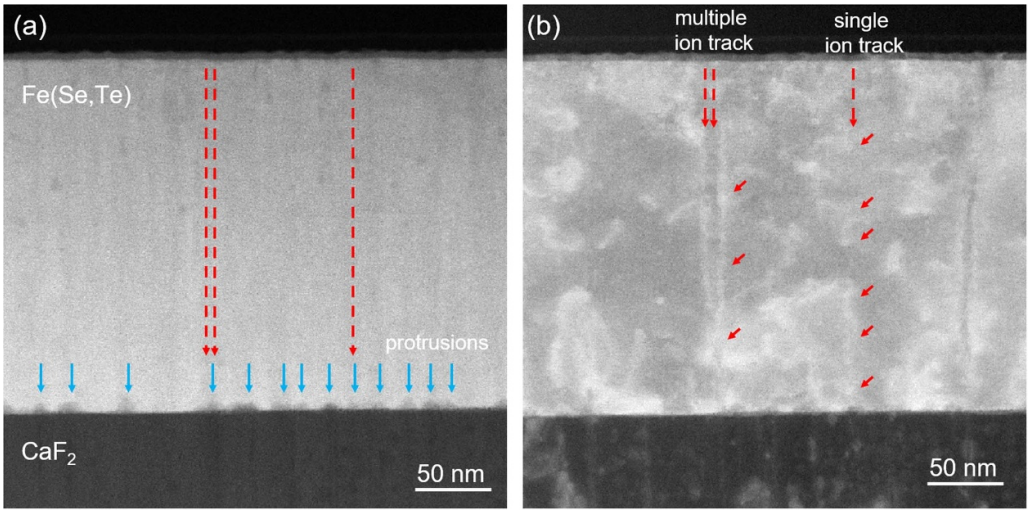

Figure 5. STEM images of the irradiated FST film. (a) HAADF-STEM image showing crater-like protrusions at the FST/CaF_2 interface (blue arrows) marking ion impact points. Red dashed arrows connect to the corresponding ion tracks shown in (b). (b) MAADF-STEM image revealing two representative ion tracks: a wide track from multiple overlapping ions (double red dashed arrows) and a narrower single-ion track (single red dashed arrow). Small red arrows guide the eye along the track development through the film thickness.

Column diameters range from a few nm up to about 10 nm, with the larger tracks that can be likely ascribed to the overlapping of multiple ion trajectories within the same column.

Comparison between the two imaging modes shows that while MAADF reveals ion tracks of varying visibility within the film, the number of detectable tracks is lower than the density of interface protrusions. This indicates that interface protrusions provide a more reliable method for assessing ion track density. However, the number of tracks counted in this way is still much lower (1.25×10^{11} cm^{-2}) than the expected nominal value and can only be considered as the lower limit of the columnar defects really induced in the FST film. An analogous difference between the nominal fluence and the density of the irradiation tracks has already been observed in other non-clean systems, as reported in [53] for Pb-ion irradiated YBCO CCs, where the authors also claim that since the irradiation tracks are scattered with a Poisson distribution, locally, their distribution can easily vary by a factor of two or three. Despite this numerical discrepancy, MAADF-STEM imaging confirms the formation of a mixed pinning landscape: pre-existing dislocations and strain-related features in the pristine film are complemented by irradiation-induced columnar defects.

To assess the functional impact of the observed microstructural changes on the superconducting properties, electrical transport measurements were performed on both pristine and irradiated samples. Figure 6 displays the temperature dependence of the electrical resistivity (normalized to the

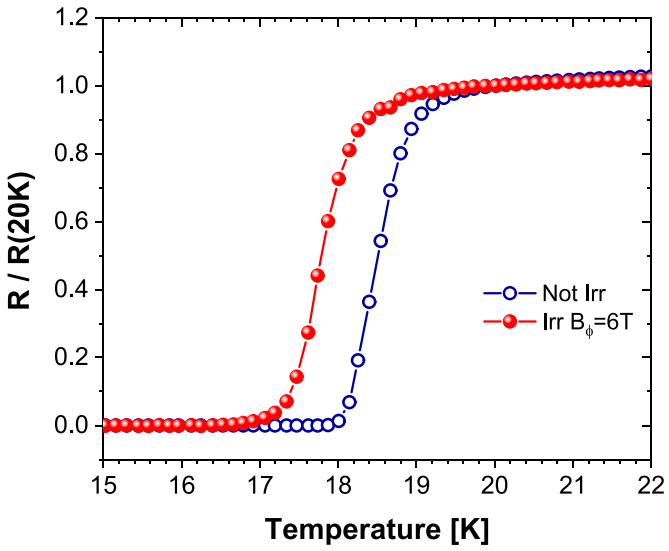

Figure 6. Temperature dependences of the normalized electrical resistivity measured at $\mu_0 H = 0$ T before and after Pb-ion irradiation.

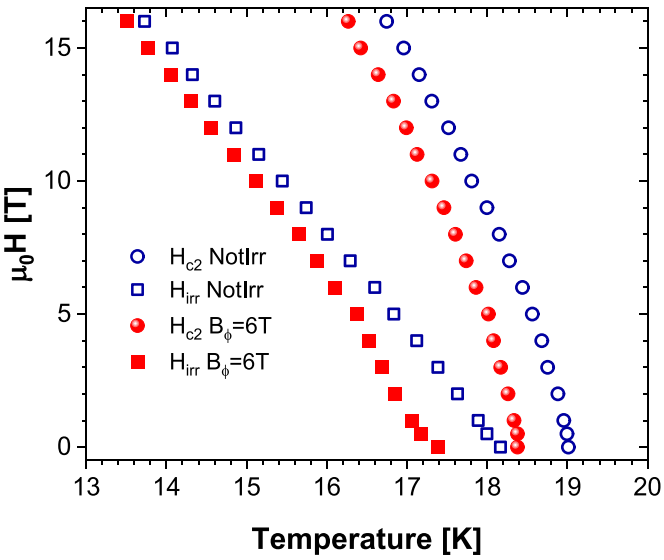

Figure 7. Temperature dependences of the upper critical field H_{c2} and the irreversibility field H_{irr} before and after Pb-ion irradiation.

value measured at 20 K) for a pristine and the Pb irradiated Hall bar when the applied field is $\mu_0 H = 0$ T. The irradiation yields a T_c decrease of about 1 K, either in the onset and in its zero-resistance value: after irradiation T_c decreases from 17.7 K to 16.5 K without transition broadening.

Most irradiation experiments on IBSs have reported a decrease in T_c [54], including high-energy heavy-ion irradiation, especially at high fluences, except for K-doped Ba-122 irradiated with 1.4 GeV Pb ions to a fluence of 10^{12} cm^{-2}, which left T_c unchanged [55]. Also, in FST films a slight decrease in T_c was usually observed [40, 41, 56], even if in some cases an increase was found after low energy proton irradiation [38, 41]. Such a modest decrease observed in T_c is compatible with the slight distortion of the crystallographic parameters calculated from HRXRD and reported in table 1.

In figure 7, the upper critical field H_{c2} and the irreversibility field H_{irr} are shown for the pristine and the irradiated bridges. The curves were obtained from the resistivity measurements, evaluating the temperature at which the resistivity equals 90% and 10% of its normal-state value, respectively. Irradiation changes the phase diagram of the FST film. Because of the decrease of the transition temperature, both the $\mu_0 H_{c2}$ and $\mu_0 H_{irr}$ curves are shifted towards lower temperature values. $\mu_0 H_{c2}$ curves, as usually reported for other irradiation experiments carried out on IBSs, exhibit the positive effect of a slight increase in scattering—i.e. a slightly larger slope dH_{c2}/dT near T_c—which has to compete with the contemporary decrease of the transition temperature [54]. The irreversibility line, after irradiation, shows a clear curvature change at $\mu_0 H_{irr} = 5$ T (i.e. 5/6 B_ϕ), where it switches from an almost parabolic behaviour at low fields to a linear one. This feature becomes particularly evident in the log–log plot $\mu_0 H_{irr}$ vs $(1-T/T_{irr,0T})$ reported in figure 8, where $T_{irr,0T}$ is the irreversibility temperature at $\mu_0 H = 0$ T. Indeed, before irradiation the curve

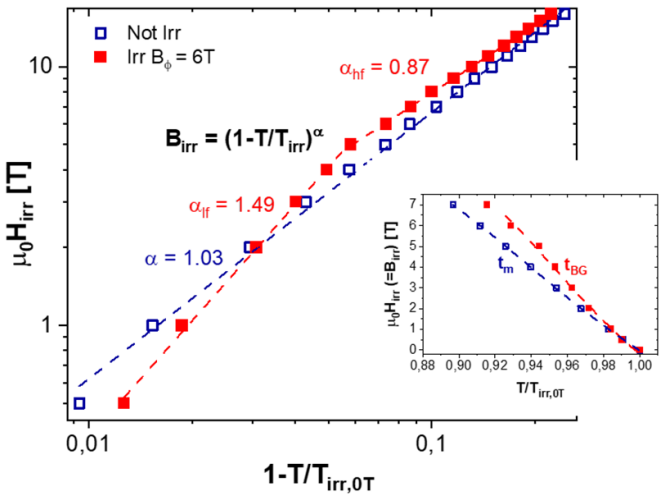

Figure 8. Double-logarithmic scale plot of irreversibility fields $\mu_0 H_{irr}$ as a function $1-T/T_{irr,0T}$. The dashed lines were achieved by fitting the experimental data (symbols) with the law $\mu_0 H_{irr} \propto (1-T/T_{irr,0T})^\alpha$. In the inset, the fit of the after-irradiation irreversibility line with (1)—see main text—is shown (t_{BG}, dashed curve). The dashed curve t_m represents the before-irradiation melting line and was obtained via a polynomial fit of the experimental data.

shows a linear behaviour with an almost constant slope in the whole investigated range of applied field while after irradiation a clear slope change emerges at $\mu_0 H_{irr} = 5$ T.

Following [57, 58], this kink could be ascribed to a crossover in flux pinning from a regime with strong vortex localization (low field region where the slope of the log–log curve is $\alpha = 1.49$ and the irreversibility line can be considered a Bose-glass transition line) to a regime with weaker vortex localization (high field region where the slope of the log–log curve is $\alpha = 0.87$). Referring to the columnar morphology of

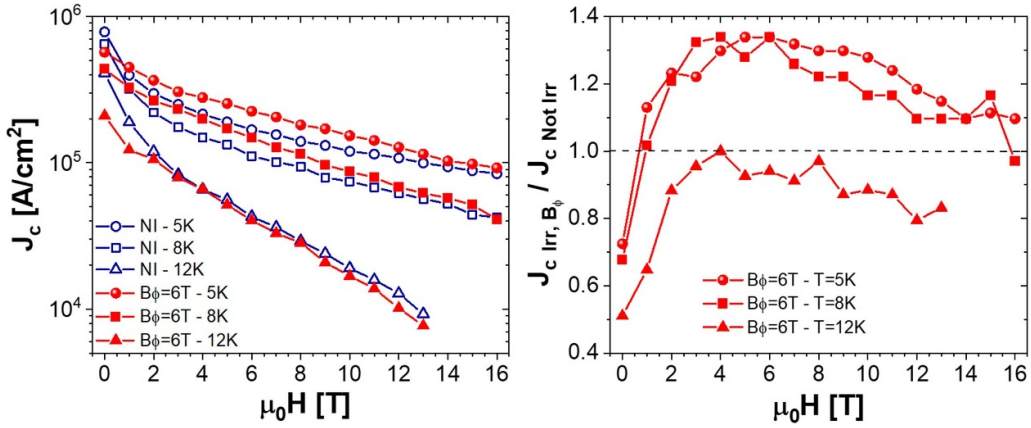

Figure 9. (a) J_c of the pristine and irradiated Hall bars measured as a function of the applied magnetic field at 5 K, 8 K, and 12 K. (b) Ratio of the critical current densities measured across the irradiated Hall bar to those measured across the pristine one at the same temperature, $T = 5$, 8 and 12 K.

irradiation-induced defects, this kink could indicate a transition from a single-vortex pinning regime provided by correlated disorder (i.e. the irradiation columnar defects) to a weaker and collective pinning regime [57, 58]. Its occurrence at a field lower than the nominal dose equivalent field can be explained by the randomness of the columns and partial overlapping of some of them, as revealed by MAADF-STEM imaging.

Within this transition hypothesis, and labelling the field at which the kink occurs as B_k, we argue that for $\mu_0 H_{irr} < B_k$, the irreversibility line can be considered a Bose-glass melting line ($T_{BG}(B)$). It can be determined as:

$$t_{BG}(B) = \frac{t_m(B) + t_{on}\gamma}{1+\gamma} \tag{1}$$

being $t_{BG}(B) = T_{BG}(B)/T_c$ and $t_m(B) = T_m(B)/T_c$ where $T_m(B)$ is the pristine melting line (assumed here equal to the irreversibility line [59]). $t_{on} = T_{on}/T_c$ and γ are the constant parameters determined by fitting the experimental data: $t_{on} = 0.991$ and $\gamma = 0.36$. As in [58], T_{on} represents the maximum temperature at which the columnar defects are effective pinning centres and γ is related to the confining diameter of the columnar defects, b_0, by the equation:

$$\gamma = \frac{b_0^2}{16 d \xi_{ab}(0)\, Gi^{1/2}} \tag{2}$$

where Gi is the Ginzburg number, and d is the average distance between the columnar tracks ($d = \sqrt{\phi_0/B_\phi} = 18.6$ nm at $B_\phi = 6$ T, assuming that all ions produce non-overlapping linear defects). Gi can be made explicit following [2, 60], then b_0 reads:

$$b_0 = \frac{\left(16\sqrt{2}\pi\,\mu_0 d k_B T_c \Gamma \lambda_{ab}(0)^2\right)^{1/2}}{\phi_0} \tag{3}$$

where k_B is the Boltzmann constant, ϕ_0 is the flux quantum and Γ is the mass anisotropy factor, here assumed to be $\Gamma = 1.7$ [61]. As for the London in-plane penetration depth, $\lambda_{ab}(0)$, we measured by a microwave method [62] $\lambda_{ab}(0) = 668$ nm in FST films with similar T_c, in good agreement with the data reported by Kurokawa *et al* [63]. Assuming all these values, from (2) we finally get $b_0 = 4.9$ nm, a value consistent with the diameter of the columnar tracks observed in high-resolution STEM images of the same sample shown in figure 5(b) [64] and the diameter of the amorphous regions created by Au-ion irradiation in Fe(Se,Te) single crystal [42].

In figure 9(a), the transport critical current density is reported as a function of magnetic field at 5, 8 and 12 K. The self-field value decreases at all temperatures, being more evident at higher temperature due to the simultaneous effect of the decrease of T_c upon irradiation. However, it is clear an increase of about 40% both at 5 and 8 K for a magnetic field range between 5 and 7 T, namely just around B_ϕ, which is a proof of the effectiveness of the irradiation process, while at higher fields the J_c is unchanged. This effect is more evident if we plot the ratio between J_c after and before irradiation as a function of the field, as reported in figure 9(b). In FST films, a 40% increase in J_c is a remarkable result. Actually, in IBS single crystals the J_c increase upon irradiation can reach much higher values, but only when starting from very clean crystals with much lower critical current densities [54]. Very few data are available specifically on FST thin films irradiated with heavy ions and only with low-energy ions: in [41], Ozaki *et al* reported an increase of about 10% upon irradiation with low energy Au ions, which induce a moderate density of isotropic cluster-like defects with sizes of the order of 10–15 nm.

The J_c improvement leads to an increase of the pinning force, $F_p = J_c \cdot \mu_0 H$ that reaches a maximum value of 1.56×10^9 N m^{-3} at $T = 5$ K and $\mu_0 H = 11$ T. At the same temperature and applied field, the before-irradiation value was 1.25×10^9 N m^{-3}. To understand the nature of the defects mainly contributing to the pinning mechanism, we investigated the dependence of pinning force F_p on the magnetic flux density. To this aim, we applied the model proposed by Dew-Hughes [65], who demonstrated the scaling of the pinning force with field:

$$F_p \propto h^p (1-h)^q \tag{4}$$

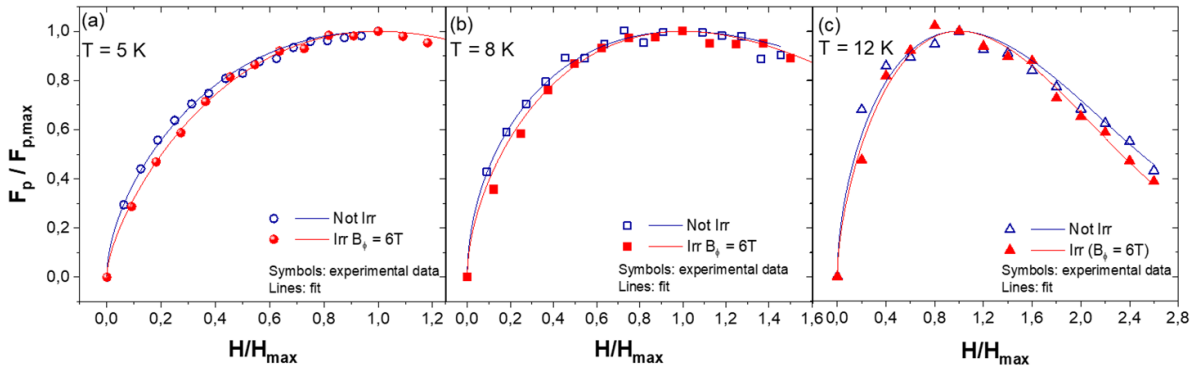

Figure 10. Magnetic flux density dependence of the normalized pinning forces measured before and after irradiation at $T = 5$ (a), 8 (b) and 12 K (c). H_{max} is the magnetic field at which the pinning force reaches its maximum value. Lines represent the fits by (5), see main text.

where $h = H/H_{irr}$ (replacing the upper critical field reported in the original relationship [66] by the irreversibility field) and the proportionality factor as well as the values of parameters p and q depend on the pinning centre type. However, since the applied field range limitations do not allow an accurate evaluation of H_{irr}, following the approach reported in [67–69] we rescaled the pinning force by $h_{max} = H/H_{max}$, where H_{max} is the magnetic field at which the pinning force reaches its maximum value, $F_{p,max}$. Based on (4), the relationship $H_{max}/H_{irr} = p/(p+q)$ can be inferred, which in turn leads to the equations:

$$F_p \propto h_{max}^{p}\left(\frac{p}{p+q}\right)^{p}\left(1-\frac{p}{p+q}h_{max}\right)^{q}$$

$$f_p = \frac{F_p}{F_{p,max}} = \left(\frac{q+p}{q}\right)^{q} h_{max}^{p}\left(1-\frac{p}{p+q}h_{max}\right)^{q}.$$

Finally, assuming that different kinds of defects can be active simultaneously [70, 71], the normalized pinning force takes the form of a direct summation:

$$f_p = \sum_{i=1}^{n} A_i \left(\frac{q_i+p_i}{q_i}\right)^{q_i} h_{max}^{p_i}\left(1-\frac{p_i}{p_i+q_i}h_{max}\right)^{q_i} \quad (5)$$

where p_i and q_i values were established 'ex ante' starting from Dew-Hughes' scaling laws [65, 72, 73] and A_i accounts for the relative contribution of each kind of defects to the total f_p.

Figure 10 shows the $f_p(h_{max})$ curves measured at $T = 5$, 8 and 12 K before and after Pb irradiation. In all cases, after irradiation a slight shift of the normalized f_p curve towards higher h_{max} can be noticed at low applied fields. This change can be attributed to the occurrence of a different pinning mechanism after irradiation. Based on defect morphology revealed by STEM analysis (figure 4(b)), we assumed the presence of both normal-core point and surface defects acting as effective pinning centres both before and after irradiation. The former could be ascribed to the presence of small dislocation, while the latter could be attributed to the presence of dislocation loops arrays. In addition, after irradiation, the contribution of linear defects is also considered. Dew-Hughes [65] does not report specific values of p and q in the case of linear pinning. However, Paturi *et al* [74] found an increase of the p parameter from 0.55 to 0.9 in YBCO films where columnar tracks were produced by 150 MeV Ag-ion irradiations. This growth is very similar to that observed by the same authors [75] in YBCO films doped with $BaZrO_3$ nanorods. In addition, a value of the p parameter close to the unity was observed by Prozorov *et al* [76] in 0.86 GeV Pb-ion irradiated YBCO films. Remarkably they found a shift of the p value from 0.96 to 0.55 tilting the sample in such a way the external field was applied parallel or perpendicular to the irradiation tracks. A reduced pinning force behaviour consistent with that expected in the case of point pinning was also found in [77] in 2 H-$NbSe_2$ single crystals irradiated with 800 MeV Xe ions. Moreover, it is worth mentioning that the assumption $q = 2$ means a δl-pinning, which is expected in the presence of strong pinning centres [78]. Based on these results, the contribution of the irradiation-induced defects in the pinning force analysis was assumed to generate the same $f_p(h)_{max}$ dependence as the normal point defects. Accordingly, for the analysis of both before- and after-irradiation curves, (5) was modified as follows

$$f_p = A\left(\frac{q_s+p_s}{q_s}\right)^{q_s} h_{max}^{p_s}\left(1-\frac{p_s}{p_s+q_s}h_{max}\right)^{q_s} + (1-A)\left(\frac{q_p+p_p}{q_p}\right)^{q_p} h_{max}^{p_p}\left(1-\frac{p_p}{p_p+q_p}h_{max}\right)^{q_p} \quad (6)$$

where $p_p = 1$, and $q_p = 2$ as in the case of normal point pinning and $p_s = 0.5$ and $q_s = 2$ as in the case of normal surface pinning [65]. The experimental data were then fitted by (6) where the parameter A provides the relative contribution of each defect morphology to the pinning force and is the only fit parameter. Notably, being the external field applied parallel to the Pb ion direction, irradiation-induced columnar defects are parallel to the applied field, too.

From fitting, we obtained that before irradiation $A = 0.66$, 0.89 and 0.72 at $T = 5$, 8 and 12 K, respectively. These results are consistent with similar investigations performed in [79], where a dominant contribution of normal surface pinning was found in FST films deposited on metallic tapes. After irradiation, the parameter A decreases becoming 0.42, 0.70 and 0.57 at $T = 5$, 8 and 12 K, respectively. This supports the evidence of a relevant contribution of the irradiation-induced defects

and of the consequent reduction of the relative contribution of the surface pinning.

4. Conclusions

In summary, we reported a thorough investigation of the effects of 1.15 GeV Pb irradiation on Fe(Se,Te) thin films grown on CaF_2 substrate. We found that, irradiation at a fluence corresponding to a dose equivalent field B_ϕ of 6 T, induces multiple types of local structural distortions including crystallographic parameter changes, enhanced microstrain, reduced coherent domain size, and formation of partially amorphized columnar defects with radial strain fields, resulting in a slight decrease in T_c while preserving long-range order. Irradiation does not significantly change the slope of $\mu_0 H_{c2}$ curves, while a clear curvature change was observed in the irreversibility line at $\mu_0 H_{irr} = 5$ T (i.e. 5/6 B_ϕ), that can be interpreted as a crossover in the flux pinning mechanism from a regime with strong vortex localization to a regime with weaker vortex localization, that is consistent with a transition from a single-vortex pinning regime provided by correlated disorder (i.e. the irradiation columnar defects observed through HAADF and MAADF-STEM imaging) to a weaker and collective pinning regime. Accordingly, at low temperature, an increase of about 40% in J_c was observed for an applied magnetic field ranging between 5 and 7 T, which is around B_ϕ. This is a demonstration of the fact that it is possible to tune J_c increase introducing a suitable amount of columnar defects—e.g. controlling the irradiation fluence of high energy heavy-ions—reaching the maximum enhancement around the matching field. The analysis of the dependence of pinning force on the magnetic field supported the evidence of a relevant contribution of the irradiation-induced columnar defects parallel to the applied field and a consequent reduction of the relative contribution of the surface pinning ascribable to the pristine defect landscape.

Data availability statement

All data that support the findings of this study are included within the article (and any supplementary files).

Acknowledgments

We acknowledge the partial financial support from the Joint Research Agreement Eni-CNR, from MUR-funded PRIN Project HIBiSCUS 201785KWLE, from Fondo Europeo di Sviluppo Regionale POR Liguria 2014–2020 Asse 1 Ricerca ed Innovazione Azione 1.5.1 Sostegno alle infrastrutture di ricerca considerate critiche/cruciali per i sistemi regionali, and from INFN-CSN5 under the experiments SAMARA and SuperMAD. Part of the experiments was carried out using the facilities of the Italian Infrastructure Beyond Nano. The staff of INFN-LNL is also gratefully acknowledged for support during irradiation experiments. M. F. acknowledges the support of the project Space It Up funded by the Italian Space Agency, ASI, and the Ministry of University and Research, MUR, under Contract No. 2024-5-E.0—CUP n. I53D24000060005.

ORCID iDs

Michela Fracasso 0000-0002-6339-4188
Mario Scuderi 0000-0001-9026-5317
Emilio Bellingeri 0000-0001-7902-0706
Andrea Malagoli 0000-0002-7204-9204
Alberto Martinelli 0000-0001-8391-3486
Nicola Manca 0000-0002-7768-2500
Laura Gozzelino 0000-0002-9204-0792
Gianluca Ghigo 0000-0003-3368-1319
Francesco Laviano 0000-0002-5271-6575
Daniele Torsello 0000-0001-9551-1716
Marina Putti 0000-0002-4529-1708
Valeria Braccini 0000-0003-0073-367X

References

[1] Kamihara Y, Watanabe T, Hirano M and Hosono H 2008 *J. Am. Chem. Soc.* **130** 3296
[2] Putti M *et al* 2010 *Supercond. Sci. Technol.* **23** 034003
[3] Gurevich A 2011 *Rep. Prog. Phys.* **74** 124501
[4] Yao C and Ma Y 2021 *iScience* **24** 102541
[5] Hsu F C *et al* 2008 *Proc. Natl Acad. Sci.* **105** 14262
[6] Hou Q, Sun L, Sun Y and Shi Z 2023 *Materials* **16** 4895
[7] Zhao J, Liao J, Dong C, Wang D and Ma Y 2024 *Materials* **17** 3059
[8] Bellingeri E, Pallecchi I, Buzio R, Gerbi A, Marré D, Cimberle M R, Tropeano M, Putti M, Palenzona A and Ferdeghini C 2010 *Appl. Phys. Lett.* **96** 102512
[9] Medvedev S *et al* 2009 *Nat. Mater.* **8** 630
[10] Bellingeri E *et al* 2014 *Supercond. Sci. Technol.* **27** 044007
[11] Iida K, Hänisch J and Yamamoto A 2020 *Supercond. Sci. Technol.* **33** 043001
[12] Iida K *et al* 2024 *Sci. Technol. Adv. Mater.* **25** 2384829
[13] Palombo M, Malagoli A, Pani M, Bernini C, Manfrinetti P, Palenzona A and Putti M 2015 *J. Appl. Phys.* **117** 213903
[14] Li X, Zhang Y, Yuan F, Zhuang J, Cao Z, Xing X, Zhou W and Shi Z 2016 *J. Alloys Compd.* **664** 218
[15] Sylva G, Augieri A, Mancini A, Rufoloni A, Vannozzi A, Celentano G, Bellingeri E, Ferdeghini C, Putti M and Braccini V 2019 *Supercond. Sci. Technol.* **32** 084006
[16] Si W, Zhou J, Jie Q, Dimitrov I, Solovyov V, Johnson P D, Jaroszynski J, Matias V, Sheehan C and Li Q 2011 *Appl. Phys. Lett.* **98** 262509
[17] Si W, Han S J, Shi X, Ehrlich S N, Jaroszynski J, Goyal A and Li Q 2013 *Nat. Commun.* **4** 1347
[18] Liu L *et al* 2023 *Adv. Eng. Mater.* **25** 2201536
[19] Mancini A, Masi A, Sung Z, Taheri B, Vannozzi A, Angrisani Armenio A, Rufoloni A, Piperno L and Celentano G 2025 *IEEE Trans. Appl. Supercond.* **35** 6601105
[20] Piperno L *et al* 2024 *iScience* **27** 111032
[21] Vannozzi A *et al* 2020 *Supercond. Sci. Technol.* **33** 084004
[22] Piperno L *et al* 2022 *IEEE Trans. Appl. Supercond.* **32** 1
[23] Lee S *et al* 2010 *Nat. Mater.* **9** 397
[24] Yuan P, Xu Z, Wang D, Zhang M, Li J and Ma Y 2017 *Supercond. Sci. Technol.* **30** 025001
[25] Sato H, Hiramatsu H, Kamiya T and Hosono H 2014 *Appl. Phys. Lett.* **104** 182603
[26] Iida K *et al* 2021 *NPG Asia Mater.* **13** 68
[27] Scuderi M, Pallecchi I, Leo A, Nigro A, Grimaldi G, Ferdeghini C, Spinella C, Guidolin M, Trotta A and Braccini V 2021 *Sci. Rep.* **11** 20100

[28] Lee S *et al* 2013 *Nat. Mater.* **12** 392
[29] Tarantini C, Kametani F, Lee S, Jiang J, Weiss J D, Jaroszynski J, Hellstrom E E, Eom C B and Larbalestier D C 2014 *Sci. Rep.* **4** 7305
[30] Seo S *et al* 2020 *NPG Asia Mater.* **12** 7
[31] Miura M, Maiorov B, Kato T, Shimode T, Wada K, Adachi S and Tanabe K 2013 *Nat. Commun.* **4** 2499
[32] Lee J *et al* 2017 *Supercond. Sci. Technol.* **30** 085006
[33] Meyer S, Langer M, Grünewald L, Hänisch J, Gerthsen D and Holzapfel B 2020 *J. Phys.: Conf. Ser.* **1559** 012052
[34] Horide T, Ichinose A, Tokura F and Matsumoto K 2021 *Thin Solid Films* **733** 138802
[35] Torsello D, Celentano G, Civale L, Corato V, Eisterer M, Gambino D, Murphy S, Speller S and Laviano F 2025 *Supercond. Sci. Technol.* **38** 053501
[36] Lang M, Djurabekova F, Medvedev N, Toulemonde M and Trautmann C 2020 Fundamental Phenomena and Applications of Swift Heavy Ion Irradiations *Comprehensive Nuclear Materials* vol 1, 2nd edn, ed R J M Konings and R E Stoller (Elsevier) pp 485–511
[37] Civale L 2025 *Supercond. Sci. Technol.* **38** 043003
[38] Ozaki T, Wu L, Zhang C, Jaroszynski J, Si W, Zhou J, Zhu Y and Li Q 2016 *Nat. Commun.* **7** 13036
[39] Torsello D *et al* 2022 *IEEE Trans. Appl. Supercond.* **32** 7500105
[40] Ozaki T, Wu L, Zhang C, Si W, Jie Q and Li Q 2018 *Supercond. Sci. Technol.* **31** 024002
[41] Ozaki T, Wu L, Gu G and Li Q 2020 *Supercond. Sci. Technol.* **33** 094008
[42] Massee F, Sprau P O, Wang Y-L, Séamus Davis J C, Ghigo G, Gu G D and Kwok W-K 2015 *Sci. Adv.* **1** e1500033
[43] Tamegai T *et al* 2012 *Supercond. Sci. Technol.* **25** 084008
[44] Torsello D, Galluzzi A, Okayasu S, Fracasso M, Gozzelino L, Tamegai T, Polichetti M and Ghigo G 2024 *Phys. Rev. B* **109** 054502
[45] Moore J D *et al* 2009 *Supercond. Sci. Technol.* **22** 125023
[46] Sun Y, Park A, Pyon S, Tamegai T, Kambara T and Ichinose A 2015 *Phys. Rev. B* **95** 104514
[47] Torsello D, Gerbaldo R, Gozzelino L, Laviano F, Takahashi A, Park A, Pyon S, Ichinose A, Tamegai T and Ghigo G 2020 *Supercond. Sci. Technol.* **33** 094012
[48] Palenzona A *et al* 2012 *Supercond. Sci. Technol.* **25** 115018
[49] Iebole M *et al* 2024 *Materials* **17** 2594
[50] Sylva G *et al* 2018 *Supercond. Sci. Technol.* **31** 054001
[51] Phillips P J, De Graef M, Kovarik L, Agrawal A, Windl W and Mills M J 2012 *Ultramicroscopy* **116** 47
[52] Oveisi E, Spadaro M C, Rotunno E, Grillo V and Hébert C 2019 *Ultramicroscopy* **200** 139
[53] Kwon J-H, Meng Y, Wu L, Zhu Y, Zhang Y, Selvamanickam V, Welp U, Kwok W-K and Zuo J-M 2018 *Supercond. Sci. Technol.* **31** 105006
[54] Eisterer M 2018 *Supercond. Sci. Technol.* **31** 013001
[55] Salovich N W *et al* 2013 *Phys. Rev. B* **87** 180502
[56] Ahmad D, Choi W J, Seo Y I, Seo S, Lee S, Park T, Mosqueira J, Gu G and Kwon Y S 2017 *New J. Phys.* **19** 093004
[57] Krusin-Elbaum L, Civale L, Blatter G, Marwick A D, Holtzberg F and Feild C 1994 *Phys. Rev. Lett.* **72** 1914
[58] Mezzetti E, Gerbaldo R, Ghigo G, Gozzelino L and Gherardi L 1999 *Phys. Rev. B* **59** 3890
[59] Čulo M *et al* 2023 *Nat. Commun.* **14** 4150
[60] Jaroszynski J *et al* 2008 *Phys. Rev. B* **78** 064511
[61] Leo A *et al* 2019 *IEEE Trans. Appl. Supercond.* **29** 7300205
[62] Ghigo G, Fracasso M, Gerbaldo R, Torsello D, Fonnesu D, Fretto M, Pira C, De Leo N and Gozzelino L 2025 *Superconductivity* **13** 100149
[63] Kurokawa H, Nakamura S, Zhao J, Shikama N, Sakishita Y, Sun Y, Nabeshima F, Imai Y, Kitano H and Maeda A 2021 *Phys. Rev. B* **104** 014505
[64] Scuderi M *et al Sci. Technol. Adv. Mater.* (Taylor & Francis Group) (in preparation)
[65] Dew-Hughes D 1974 *Phil. Mag.* **30** 293
[66] Koblischka M R, van Dalen A J J, Higuchi T, Yoo S I and Murakami M 1998 *Phys. Rev. B* **58** 2863
[67] Higuchi T, Yoo S I and Murakami M 1999 *Phys. Rev. B* **59** 1514
[68] Ye J, Mou S, Zhu R, Liu L and Li Y 2022 *J. Appl. Phys.* **132** 013902
[69] Zhang J, Hänisch J, Yang X S, Zhao K and Zhao Y 2023 *Supercond. Sci. Technol.* **36** 025008
[70] Gozzelino L, Gerbaldo R, Ghigo G, Mezzetti E, Minetti B, Carlino E, Krabbes G, Schaetzle P, Cuttone G and Rovelli A 1999 *Supercond. Sci. Technol.* **12** 1075
[71] Crisan A, Dang V S, Yearwood G, Mikheenko P, Huhtinen H and Paturi P 2014 *Physica C* **503** 89
[72] Leo A *et al* 2015 *Supercond. Sci. Technol.* **28** 125001
[73] Koblischka M R and Muralidhar M 2016 *Int. J. Mod. Phys.* **30** 1630017
[74] Paturi P, Aye M M, Soman A, Notthoff C, Kluth P, Strickland N and Huhtinen H 2025 *IEEE Trans. Appl. Supercond.* **35** 8000105
[75] Paturi P, Malmivirta M, Palonen H and Huhtinen H 2016 *IEEE Trans. Appl. Supercond.* **26** 8000705
[76] Prozorov R, Tsameret A, Yeshurun Y, Koren G, Konczykowski M and Bouffard S 1994 *Physica C* **234** 311
[77] Li W J, Pyon S, Takahashi A, Miyawaki D, Kobayashi Y and Tamegai T 2020 *J. Phys.: Conf. Ser.* **1590** 012003
[78] Shahbazi M, Wang X L, Choi K Y and Dou S X 2013 *Appl. Phys. Lett.* **103** 032605
[79] Mou S, Ye J, Zhu R, Li R, Liu L and Li Y 2024 *J. Am. Ceram. Soc.* **107** 144